

Practical Collaborative Perception: A Framework for Asynchronous and Multi-Agent 3D Object Detection

Minh-Quan Dao¹, Julie Stephany Berrio², Vincent Fremont¹, Mao Shan², Elwan Hery¹, and Stewart Worrall²

arXiv:2307.01462v1 [cs.RO] 4 Jul 2023

Abstract—In this paper, we improve the single-vehicle 3D object detection models using LiDAR by extending their capacity to process point cloud sequences instead of individual point clouds. In this step, we extend our previous work [1] on rectification of the shadow effect in the concatenation of point clouds to boost the detection accuracy of multi-frame detection models. Our extension includes incorporating HD Map and distilling an Oracle model. Next, we further increase the performance of single-vehicle perception using multi-agent collaboration via Vehicle-to-everything (V2X) communication. We devise a simple yet effective collaboration method that achieves better bandwidth-performance tradeoffs than prior arts while minimizing changes made to single-vehicle detection models and assumptions on inter-agent synchronization. Experiments on the V2X-Sim dataset show that our collaboration method achieves 98% performance of the early collaboration while consuming the equivalent amount of bandwidth usage of late collaboration which is 0.03% of early collaboration. The code will be released at <https://github.com/quan-dao/practical-collab-perception>

Index Terms—V2X Collaborative Perception, 3D Object Detection, Scene Flow.

I. INTRODUCTION

Object detection, which amounts to localizing objects as 3D bounding boxes, is a fundamental autonomous driving software stack module. It provides input to downstream tasks such as object tracking, motion forecast, and navigation. Due to the need for accurately localizing objects in 3D, state-of-the-art methods use LiDARs as the primary sensing modality. While significant advancements have been made, two challenges continuously plague LiDAR-based detection models: occlusion and sparsity, especially at long ranges.

As occluded objects in one frame can be visible in others due to their motion and/or the ego vehicle’s motion, and sparse regions can become dense as the ego vehicle approaches, the utilization of point cloud sequences is an appealing candidate for boosting the boundary of 3D object detection. First introduced in [2] as a means for alleviating the extreme sparsity of point clouds obtained by a 32-beam LiDAR, the concatenation of point cloud sequences using ego vehicle pose; thus the name Ego Motion Compensation (EMC), is by far the most popular multi-frame method due to its simplicity. Yet, being highly effective [3]–[7]. More recent works such

This work has been supported by the French-Australian Science and Innovation Collaboration (FASIC) and the Australian Centre for Robotics (ACFR). The authors are with Ecole centrale de Nantes¹ (France). E-mails: {minh-quan.dao, vincent.fremont, elwan.hery}@ls2n.fr and the ACFR at the University of Sydney² (Australia). E-mails: ² {j.berrio, m.shan, s.worrall}@acfr.usyd.edu.au

as 3D-MAN [8], MoDAR [9], and MPPNet [10] are built upon this concept by dividing the input sequence into several subsequences whose point clouds are concatenated to produce preliminary detections. These preliminary detections are then fused to result in the final detections.

The major drawback of EMC-concatenated point clouds is that their formulation only accounts for the motion of the ego vehicle while ignoring the motion of dynamic objects, thus their instantiating at multiple locations, which is referred to use the shadow effect [11], during the observation horizon as can be seen in Fig.1. This effect, which is essentially a misalignment in 3D space between objects’ points and their location, results in a misalignment in feature spaces such as on the bird-eye view image, limiting the performance gain brought by an increased number of points (thanks to point cloud concatenation) to stationary and slow-moving objects [8]. In our previous work [1], we resolved this alignment explicitly by rectifying concatenated point clouds using estimated point-wise scene flow. The add-on module named *Aligner*, which we proposed, achieved competitive scene flow performance while substantially improving the detection accuracy, especially of large objects with a severe shadow effect.

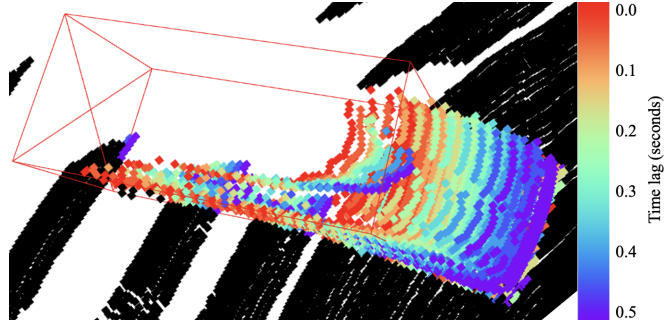


Fig. 1. A dynamic car’s appearance on the concatenation of a 10-point-cloud sequence spanning 0.5 seconds. Points are colour-coded according to their time lag with respect to the present.

Despite the power of point cloud sequences, the issue of occlusion and sparsity at long range persists as several regions remain invisible to the ego vehicle due to the geometry of the scene (e.g., a large object obstructs the ego vehicle’s field of view) or the traffic rule that limits the ego vehicle’s motion (e.g., the ego vehicle must stop at a red light). These issues can be safety critical when the ego vehicle navigates complex traffic, such as at intersections where a Waymo report indicates that a quarter of severe accidents involving their autonomous

vehicles are due to occlusion [12]. Therefore, in this work, we aim to boost further object detection made by a single-vehicle operating on point cloud sequences using the Vehicle-to-everything (V2X) collaborative perception.

In the collaborative perception framework via V2X, Intelligent Road-Side Units (IRSUs), which are equipped with advanced sensing systems (e.g., comparable to an autonomous vehicle) and located at elevated locations that maximize their field of view, and other vehicles can make measurements in regions that are inaccessible or partially occluded to others. Together they can come up with a complete representation of the environment. The enhanced perception capacity, thanks to V2X, comes with several new technical challenges; the most notorious among them is the performance-bandwidth tradeoff which revolves around two questions (i) which information to be broadcasted and (ii) how to fuse the exchanged information.

This tradeoff establishes a design spectrum ranging from *early collaboration*, which exchanges raw sensory measurements - point clouds in the context of this paper, thus consuming the maximum bandwidth, to achieve the maximal performance to *late collaboration* that exchanges outputs (e.g., object detection as 3D bounding boxes) to achieves minimal bandwidth usage at the expense of limited performance. Naturally, researches on V2X collaboration frameworks [13]–[16] are drawn toward the middle of this spectrum, thus the category's name of *mid-collaboration*, where intermediate representations such as bird-eye view (BEV) images of agents' surrounding environment are chosen for broadcasting in an attempt of balancing the two mutually excluding design targets. While the motivation is just, most mid-collaboration methods require making substantial changes to the architecture of single-agent perception models to accommodate the fusion module where the combination of exchanged representations takes place. More importantly, most methods make strong assumptions about the synchronization among connected agents. For example, DiscoNet [14] considers a perfectly synced setting where agents share the same clock, collect and process point clouds at the same rate and the transmission/ receiving of BEV images experience zero latency. V2VNet [13] and ViT-V2X [15] account for latency by postulating a global misalignment between exchanged BEV images and the BEV image of the ego vehicle caused by the movement of the ego vehicle between the time step it makes the requests for BEV images and the time step the exchanged BEV images are received. This means these works implicitly assume agents in the V2X network obtain point clouds synchronously.

Taking a different approach to mid-collaboration, we aim for a more practical collaboration framework that emphasizes minimal

- Bandwidth consumption
- Changes made to single-agent models
- Inter-agent synchronization assumption

We ground our design at minimal bandwidth consumption which can only be achieved by exchanging agents' output which detected objects. This design choice naturally satisfies the second design target as it dismisses the need for complex mid-representation fusion modules. We achieve the final target

by only assuming that connected agents share a common time reference which is practically achievable using GPS time.

The challenge posed by our relaxed inter-agent synchronization assumption is that information (i.e., detected objects) broadcasted by agents in the V2X network may never have the same timestamp as the query made by the ego vehicle. In other words, the detections made by other agents that are available on the V2X network always have an older timestamp compared to the current timestamp of the ego vehicle. This timestamp mismatch results in a misalignment between exchanged detected objects and their associated ground truths (if the detections are true positive). We resolve this misalignment by predicting objects' velocities simultaneously with their poses using the *Aligner* module developed by our previous work [1]. Specifically, each detected object pools point-wise scene flow produced by the *Aligner* to compute its velocity, which is then used to propagate this object from one timestamp to another. As the scene flow plays a more critical role in the V2X collaborative perception, we first extend our *Aligner* by incorporating HD Maps into its framework and improving its supervision by distilling an Oracle model (details are in Sec.III-A2). The resulting module is dubbed *Aligner++*.

Aware of the limitation of the late collaboration whose details are presented in Sec.II, we derive a novel collaboration strategy that fuses detections made by connected agents at a past timestamp with the current point cloud acquired by the ego vehicle using inspiration from the recent advance in multi-frame single-vehicle object detection [9].

This paper makes the following contributions:

- Extending our previous work [1] to further boosts single-vehicle object detection accuracy and achieves more accurate scene flow prediction
- Deriving a practical framework for V2X collaborative perception that consumes minimal bandwidth while achieving competitive performance compared to the early collaboration in the perfect synchronization setting
- Performing extensive evaluations on NuScenes [2], KITTI [17], and V2X-Sim [18] dataset to verify our method

II. RELATED WORKS

A V2X cooperative perception framework comprises two main components connected autonomous vehicles (CAVs) and intelligent roadside units (IRSUs), both equipped with advanced sensing systems to perceive their environment. IRSUs are stationary installed at elevated positions to obtain minimally occluded fields of view. CAVs and IRSUs can exchange information to enhance their perception capacity (e.g., seeing beyond occlusion). In the context of this work, the sensing system of CAVs and IRSUs is restricted to a single LiDAR and the perception task focuses on 3D object detection.

As described in the previous section, the main challenge of V2X cooperative perception is the performance-bandwidth tradeoff which establishes a design spectrum ranging from early to late collaboration. In the *early collaboration* approach, as depicted in Fig.2, agents exchange their raw measurements - point clouds. At every timestep, the ego vehicle concatenates its own point cloud with those obtained by other CAVs and

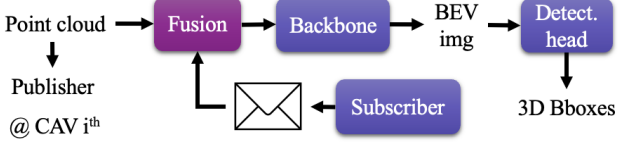


Fig. 2. Architecture of the early collaboration.

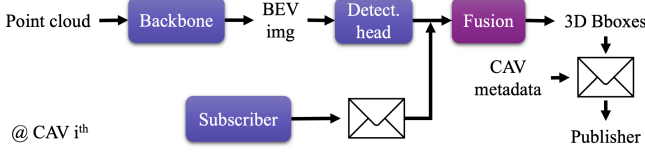


Fig. 3. Architecture of the late collaboration.

IRSUs to form the input for its perception module. This combined point cloud offers a comprehensive view of the scene with minimal occlusion and sparsity thanks to the diverse perspectives of connected agents, thus being regarded as the upper bound of the performance of the V2X collaborative perception [18], [19]. However, due to the significant amount of bandwidth required to transmit raw point clouds (the order of 10 MB), the early collaboration strategy is not feasible for real-world deployments.

On the other extreme of the performance-bandwidth trade-off, the *late collaboration* approach focuses on minimizing bandwidth usage by exchanging only the agents' predictions, specifically the detection results in the form of 3D bounding boxes. As illustrated in Fig.3, each agent independently conducts object detection on its own point cloud. Subsequently, the agent merges its own predictions with those made by others to generate the final output. While this strategy is more feasible for real-world deployments thanks to its minimal bandwidth consumption, it exhibits significantly lower performance gains compared to early fusion. The limited interaction among agents in the late collaboration approach contributes to this inferior performance. In noisy environments where latency is a factor, the late collaboration strategy even underperforms single-vehicle perception [15].

The *mid-collaboration* strategy aims to find a balance between performance and bandwidth consumption by exchanging intermediate scene representations generated by the backbone of the agents' perception model. The motivation behind this approach is that the intermediate scene representation contains more contextual information compared to the final output (i.e., 3D bounding boxes), enabling deeper interaction among agents. Moreover, this representation is more compact than raw point clouds since it has been reduced in size through a series of convolution layers in the backbone. It can also be further compressed using an autoencoder to minimize bandwidth usage. While the idea is elegant, implementing the intermediate collaboration strategy requires a range of modules, shown in Figure 4, including compressor, decompressor, and representation fusion, among others, to match the performance of early collaboration. The fusion, in particular, is quite intricate as it involves learnable collaboration graphs

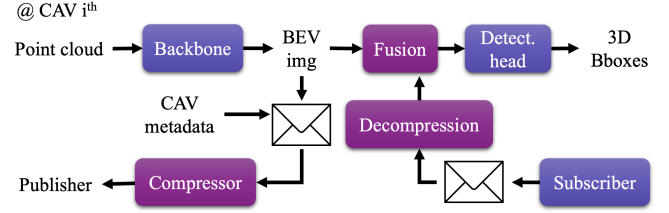


Fig. 4. V2X Cooperative Perception via the Mid-fusion architecture.

using techniques such as Graph Neural Networks [13], [14] or Transformers [15] to effectively fuse exchanged representations. Furthermore, dedicated modules are required to account for different practical challenges. For example, [13], [15] use the Spatial Transformer [20] to resolve the global misalignment between the ego vehicle's representation and others' caused by the ego vehicle's motion between when it makes the query and when it receives exchanged information. In [16], the Fused Axial Attention [21] is used to bridge the domain gap between representations made by different detection models (e.g., PointPillar [22] and VoxelNet [23]) used by different agents in the V2X network. More importantly, most mid-collaboration methods make strong assumptions about inter-agent synchronization which is either (i) perfect synchronization where exchanged representations always share the same timestamp [14] or (ii) synchronized point cloud acquisitions, meaning all agents obtain and process point clouds at the same rate and at the same time [13], [15]. Because of these complexities, the real-world deployment of intermediate fusion remains challenging.

In this work, we aim to resolve the aforementioned complexities of mid-collaboration to obtain a practical framework for V2X collaborative perception. Our design is grounded in minimal bandwidth consumption as this is nonnegotiable in real-world deployment. To achieve this design goal, we choose object detection, in the form of 3D bounding boxes, as the information to be exchanged, which is similar to the *late collaboration* strategy. We further relax the assumption on inter-agent synchronization to agents sharing a common time reference (e.g., GPS time) and acknowledge that agents produce detections at different rates. As a result, exchanged detections always have older timestamps compared to the timestamp of the query made by the ego vehicle, thus risking a spatial misalignment between exchanged detections and their associated ground truth (if detections are true positive). We resolve this misalignment by predicting objects' velocity simultaneously with their locations by pooling point-wise scene flow which can be produced by integrating our *Aligner++* module to any off-the-shelf BEV-based object detectors. Finally, we avoid the inferior performance of *late collaboration* by devising a new collaboration strategy that fuses exchanged detections with the ego vehicle's raw point cloud for subsequent processing using its detection model rather than fusing exchanged detections with detections made by the ego vehicle. An illustration of our approach is presented in Fig.5.

The innovation of our collaboration strategy lies in recogniz-

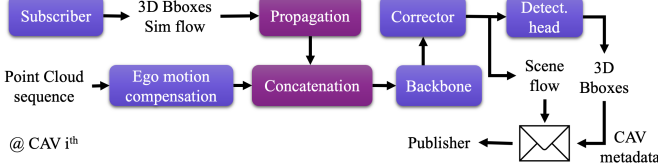


Fig. 5. Our V2X Cooperative Perception.

ing the similarity between object detection using point cloud sequences and collaborative detection. In both cases, there is a need to fuse information obtained from diverse perspectives. Point cloud sequences involve capturing the motion of the ego vehicle, which results in varying viewpoints, while collaborative detection entails incorporating insights from other agents present in the environment. By drawing this parallel, we leverage the shared principle of fusing information from multiple perspectives to enhance the accuracy and robustness of both object detection approaches

III. METHODOLOGY

This section first presents the extension we introduce to our previous work [1] to improve the scene flow estimation as well as further boost the performance gain when integrating our module to single-vehicle object detection models. Next, our strategy for V2X collaborative perception that enables using asynchronous exchanged information is derived.

A. Improving Single-Vehicle Perception

As mentioned in Sec.I, the accuracy of single-vehicle detection can be significantly improved by using the concatenation point cloud sequences as inputs. However, such concatenation is done by the Ego Motion Compensation method which only accounts for the motion of the ego vehicle resulting in the shadow effect (Fig.1) in the concatenated point cloud. This effect, which is a misalignment in the 3D space between objects' points and their locations, leads to a misalignment in feature spaces (e.g., BEV representations), thus degrading detection accuracy for dynamic objects. In this section, we recall the approach we use in [1] to handle this effect and present the extensions we make to it.

1) *Shadow Effect: Cause and Rectification:* Let $\mathcal{P}^t = \{\mathbf{p}_j^t = [x, y, z, r, \Delta] \mid j = 1, \dots, N\}$ denote a point cloud collected by the ego vehicle at time step t . Here, each point \mathbf{p}_j has two features namely reflectant r and time-lag Δ with respect to a predefined time step. The point cloud is expressed in the ego vehicle frame $\mathcal{E}(t)$ measured with respect to a global frame \mathcal{G} . To concatenate a point cloud sequence $\mathcal{S} = \{\mathcal{P}^{t-K}, \mathcal{P}^{t-K+1}, \dots, \mathcal{P}^t\}$ of length $K+1$, each point of point cloud $\mathcal{P}^{t-\Delta t}$ is transformed to the global frame using the ego vehicle pose at the same time step as in (1), hence the method's name Ego Motion Compensation (EMC).

$$\mathcal{G}\mathbf{p}_i^{t-\Delta t} = \mathcal{G}\mathbf{T}_{\mathcal{E}(t-\Delta t)} \cdot \mathbf{p}_i^{t-\Delta t} \quad (1)$$

Here, $\mathcal{G}\mathbf{T}_s \in \mathbf{SE}(3)$ represents the rigid transformation that maps points in frame s to frame d . EMC undoes the motion of the ego vehicle; however, it fails to account for objects'

motion. As a result, the appearance of a dynamic object in the concatenated point cloud comprises several instances, each corresponding to the object's poses in the global frame at a particular time step, as in Fig.1.

Such distortion can be rectified by first transforming an object's points collected at different time steps to its body frame, and then from to the global frame at the desired time step. This two-step transformation is illustrated in (2).

$$\mathcal{G}\hat{\mathbf{p}}^{t-\Delta t} = \mathcal{G}\mathbf{T}_{\mathcal{O}(t)} \cdot \mathcal{O}(t-\Delta t)\mathbf{T}_{\mathcal{G}} \cdot \mathcal{G}\mathbf{p}^{t-\Delta t} \quad (2)$$

Here, $\mathcal{O}(t)$ represents the object frame at time t . The point's subscript is omitted for clarity.

Equation (2) implies that $\mathcal{O}(t)\mathbf{T}_{\mathcal{O}(t-\Delta t)}$ is the identity transformation, which is the case for rigid objects. More importantly, the computation of the *rectification transformation*, $\mathcal{G}\mathbf{T}_{\mathcal{O}(t)} \cdot \mathcal{O}(t-\Delta t)\mathbf{T}_{\mathcal{G}}$, requires object poses which are not available at test time. Our previous work [1] develops a model that estimates such transformation directly from the concatenation of point cloud sequences. The following section briefly recalls the method used in [1] and presents our extension.

2) *Learning to Rectify the Shadow Effect:* In [1], we propose a drop-in module, named *Aligner*, for 3D object detection models that create a Bird-Eye View (BEV) representation, $\mathbf{B} \in \mathbb{R}^{C \times H \times W}$, of the scene as an intermediate output. Our module first computes the feature of $\mathbf{f}_i \in \mathbb{R}^C$ of a point \mathbf{p}_i by bilinear interpolating on \mathbf{B} using its projection to the BEV. Each point feature is then decoded into the point's scene flow $\mathbf{d}_i \in \mathbb{R}^3$ representing how much this point needs to offset to rectify the shadow effect. After being rectified, the new point cloud is used to scatter the set of point features $\{\mathbf{f}_i\}$ to the BEV to obtain a new BEV image \mathbf{B}' . While undergoing minimized impact of the shadow effect thanks to the rectification, \mathbf{B}' is sparse as only occupied pillars have features, which has a negative effect on detection accuracy [24]. On the other hand, \mathbf{B} is semi-dense thanks to the occupancy leakage caused by the convolutions in the detection models' backbone but possesses feature misalignment due to the shadow effect. To utilize the best of the two representations, they are fused before being fed to the Region Proposal Networks (RPN) for 3D bounding boxes. The complete pipeline is summarized in Fig.6.

The learning target \mathbf{d}^* for the scene flow \mathbf{d} of a point $\mathbf{p}^{t-\Delta t}$, which has the timestamp $(t - \Delta t)$ (i.e., collected at time step $t - \Delta t$), is the difference between its location and its rectified location computed by (2).

$$\mathbf{d}^* = \mathcal{G}\hat{\mathbf{p}}^{t-\Delta t} - \mathcal{G}\mathbf{p}^{t-\Delta t} \quad (3)$$

A 3D bounding box is parameterized by a seven-vector comprised of its center coordinate $[c_x, c_y, c_z]$, its size $[l, w, h]$, and its heading θ . The learning target is defined according to the framework which the RPN follows (e.g., anchor-based [25] or center-based [4]).

To improve the accuracy of [1] in estimating scene flow, thus ultimately improving object detection, we introduce two extensions (i) incorporating HD Map and (ii) distilling an Oracle model. Previous works in integrating HD Maps into 3D object detection models ([26], [27]) opt for a mid-fusion approach that concatenates rasterized maps with backbone-made BEV

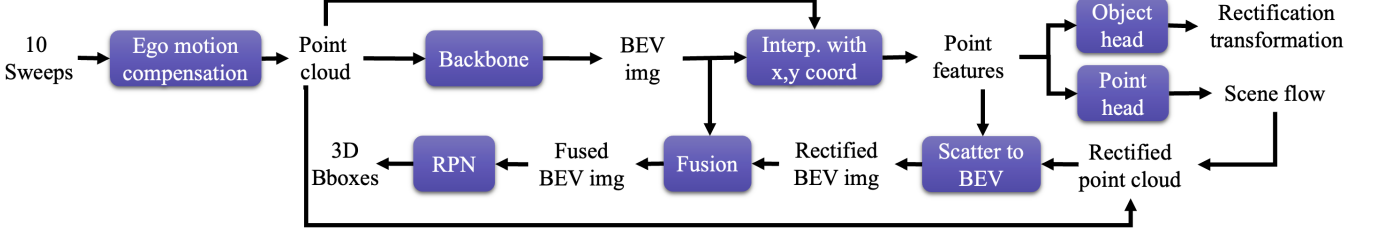


Fig. 6. Aligner

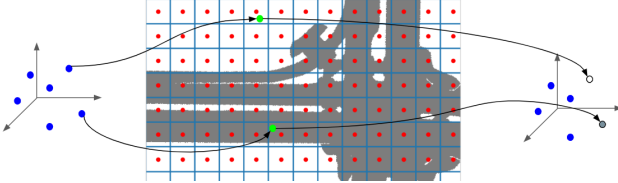


Fig. 7. Extracting map features for points.

representations. However, this approach is incompatible with copy-paste data augmentation [25], which randomly samples ground truth objects from a database and pastes them to each point cloud used for training, as pasted objects do not necessarily adhere to the semantics and geometry of the map (e.g., cars appear inside a building). Moreover, they only utilize the map's binary channels such as drivable areas, sidewalks, or car parks while omitting the lane direction which is potentially helpful for estimating scene flow and objects' heading direction.

Aware of these two limitations, we propose to extract the map feature for each 3D point and use it to augment the point's raw features prior to further processing (e.g., building a ground truth database or computing a BEV representation for object detection). The map feature extraction process is illustrated in Fig.7 where points' coordinate in the map's BEV is used for nearest neighbor interpolation. This attachment of the map features to points results in an early fusion between HD Maps and LiDARs, rendering the concatenation of maps' channels to backbone-made BEV representations unnecessary. As a result, HD Maps are made compatible with copy-paste data augmentation.

To improve the quality of the fused BEV representation, \mathbf{B}^f in Fig.6, in terms of minimizing the feature misalignment caused by the shadow effect and reducing the sparsity, we use the teacher-student framework shown in Fig.8. In detail, we use ground truth objects' trajectories to rectify the concatenation of point cloud sequences and use the shadow-effect-free results, illustrated in Fig.9, to train a teacher model. After the teacher converged, its BEV representation \mathbf{B}^t is used to guide the student's fused BEV representation \mathbf{B}^f by optimizing the students' weight so that the difference measured by the L_2 loss between these two representations is minimized.

B. V2X Collaborative Perception Framework

The V2X setting that we target in this paper comprises multiple CAVs and IRSUs which are collectively referred

to as agents. An agent \mathcal{A}_i is equipped with a LiDAR to localize in a common global frame \mathcal{G} and detect objects in its surrounding environment. The detection is based on the processing of point cloud sequences using a detection model made of the integration of the *Aligner++* presented in the Sec.III-A2 into an off-the-shelf single-frame object detector such as PointPillar [22]. At a time step t_i , agent \mathcal{A}_i uses a K -point-cloud sequence $\mathcal{S}_i = \{\mathcal{P}_i^{t_i-K+1}, \dots, \mathcal{P}_i^{t_i}\}$ as an input to its detection model. An object $b_{i,j}$ detected by agent \mathcal{A}_i is parameterized by a nine-vector $[x, y, z, w, l, h, \theta, s, c]$. The first seven numbers localize the object by its center location $[x, y, z]$, size $[w, l, h]$, heading direction θ . The last two numbers s and c respectively denote confidence score s and the predicted class c .

Upon receiving a query having timestamp t , agent \mathcal{A}_i will communicate its detection $\mathcal{B}_i^{t_i} = \{\mathbf{b}_{i,j}\}_{j=1}^{M_i}$ and metadata produced timestamp t_i that is prior to and closest to t . The agent's metadata produced at a timestamp t_i is made of the timestamp itself and the agent's pose $\mathcal{E}_i(t_i)$ at this timestamp.

Given this setting, we aim to enhance the ego vehicle's capacity of detecting objects by fusing its point cloud sequence $\mathcal{S}_e = \{\mathcal{P}_e^{t-K+1}, \dots, \mathcal{P}_e^t\}$ with the *MoDAR* interpretation of predictions $\mathcal{B}_i^{t_i}$ made by other agents. The following section provides an overview of the origin of *MoDAR* and presents in detail how we adapt this concept to collaborative perception via the V2X context.

1) MoDAR for Object Detection on Point Cloud Sequences:

MoDAR is created to enable detecting objects in extremely long point cloud sequences (hundreds of frames). In the *MoDAR* framework, a sequence is divided into several short sequences where objects are detected by a single-frame detector, tracked by a simple multi-object tracktor (e.g., [28]). Then, the data-driven motion forecasting model MultiPath++ [29] predicts objects' future poses based on objects' trajectories established by the tracktor. Using prediction about objects' future poses, detected objects in each short subsequence are propagated to the desired time step (e.g., the present). Next, each propagated object, which is represented as an up-right 3D bounding box (parameterized by the location of its center, size, and heading) with a confidence score and a class, is interpreted into a 3D point that takes the box's center as its coordinate and the box's size, heading, confidence score and class as features. These points interpreted from 3D bounding boxes are referred to as *MoDAR* points. They enable packing an entire subsequence into a small number of points, thus enabling an efficient fusion of extremely long point cloud sequences.

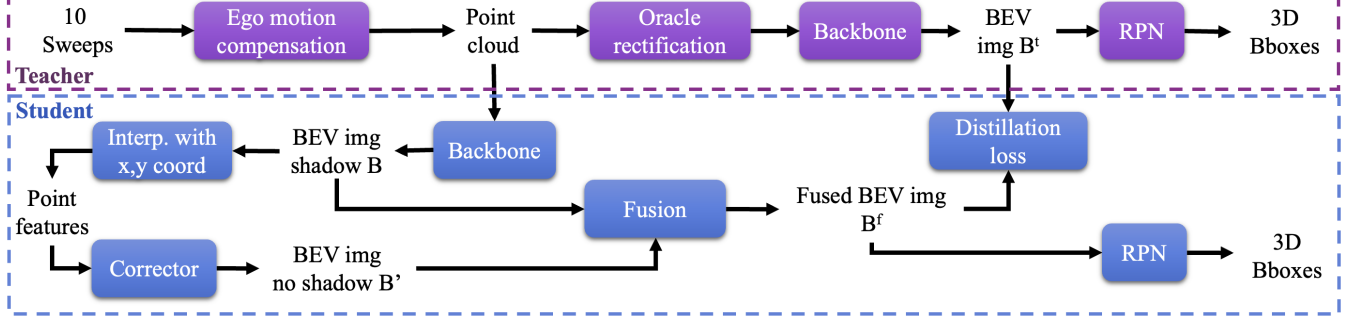


Fig. 8. Alinger++'s Teacher-student framework

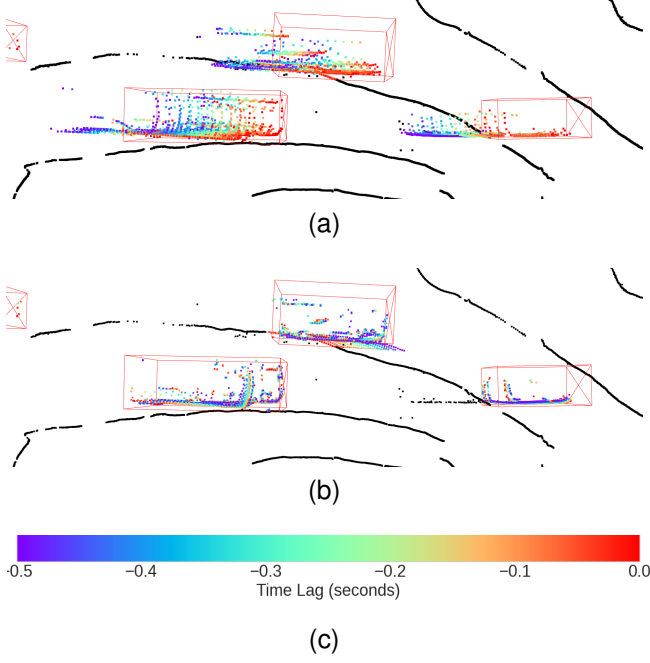


Fig. 9. Comparison between concatenation of a point cloud sequence (a) and its rectification using objects' ground truth trajectories (b). Points are color-coded according to their time-lag with respect to the present. The color bar is shown in (c).

2) *V2X Collaboration using MoDAR Points*: We draw the following similarity between single-vehicle object detection on point cloud sequences and V2X collaborative detection: these two tasks share the common challenge of finding an effective method for fusing information obtained from different perspectives caused by the motion of the ego vehicle in the case of point cloud sequences and the presence of other agents in the case of collaboration via V2X. Based on this observation, we use *MoDAR* points as the medium for conveying information among agents in the V2X network. Specifically, we interpret an object detected by agent \mathcal{A}_i as a 3D bounding box $\mathbf{b}_{i,j} = [x, y, z, w, l, h, \theta, s, c]$ to a *MoDAR* point $\mathbf{m}_{i,j}$ by assigning

- $[x, y, z]$ to the coordinate of $\mathbf{m}_{i,j}$
- $[w, l, h, \theta, s, c]$ to $\mathbf{m}_{i,j}$'s features

The challenge in our V2X setting is that different agents detect objects at different rates, thus forcing the ego vehicle

to utilize *MoDAR* points made by other agents at passed time steps. This timestamp mismatch results in a spatial misalignment between exchanged *MoDAR* points and ground truth dynamic objects, which can diminish the benefit of collaboration or even decrease the ego vehicle's accuracy. This challenge is encountered in the context of single-vehicle detection on point cloud sequences as well because dynamic objects change their poses from one subsequence to another. [9] resolves this by predicting objects' pose using a multi-object tracker and the motion forecasting model MultiPath++.

While this is feasible in the V2X context, the implementation of add-on modules for future pose prediction does not align with our design target of minimal architecture. Instead, we use the scene flow to propagate *MoDAR* points from a passed timestep to the timestep queried by the ego vehicle. Since *MoDAR* points are virtual, their scene flow is not estimated directly from a point cloud sequence but is aggregated from the scene flow of points residing in the box they represent. To be concrete, let $\mathbf{m}_{i,j}$ be a *MoDAR* point representing a 3D bounding box $\mathbf{B}_{i,j}$ detected by agent \mathcal{A}_i at timestep t_i . $\mathbf{p}_{i,h}$ and $\mathbf{f}_{i,h}$ respectively denote a real 3D point in the concatenation of agent \mathcal{A}_i 's point cloud sequence \mathcal{S}_i and its predicted scene flow. The scene flow $\mathbf{f}_{i,j}^m$ of $\mathbf{m}_{i,j}$ is computed by

$$\mathbf{f}_{i,j}^m = \text{mean} \{ \mathbf{f}_{i,h} \mid \mathbf{p}_{i,h} \in \mathbf{B}_{i,j} \} \quad (4)$$

Once its scene flow is obtained, the *MoDAR* point $\mathbf{m}_{i,j}$ is propagated to the timestep t queried by the ego vehicle as following

$$[\hat{\mathbf{m}}_{i,j}]_{x,y,z} = [\mathbf{m}_{i,j}]_{x,y,z} + \frac{t - t_i}{|\mathcal{S}_i|} \mathbf{f}_{i,j}^m \quad (5)$$

Here, $|\mathcal{S}_i|$ denotes the length of the point cloud sequence \mathcal{S}_i measured in seconds. $[\cdot]_{x,y,z}$ is the operator that extracts 3D coordinate of a *MoDAR* point.

Finally, propagated *MoDAR* point is transformed from the agent \mathcal{A}_i 's pose $\mathcal{E}_i(t_i)$ at time step t_i to the ego vehicle pose $\mathcal{E}_e(t)$ at time step t using the localization in the common global frame \mathcal{G} of the two agents

$${}^{\mathcal{E}_e(t)}[\hat{\mathbf{m}}_{i,j}]_{x,y,z} = {}^{\mathcal{G}}\mathbf{T}_{\mathcal{E}_e(t)}^{-1} {}^{\mathcal{G}}\mathbf{T}_{\mathcal{E}_i(t_i)} [\hat{\mathbf{m}}_{i,j}]_{x,y,z} \quad (6)$$

The concatenation between the set of *MoDAR* points received from other agents and the ego vehicle's raw point cloud

(resulting from concatenating its own point cloud sequence) is done straightforwardly by padding

- points in the ego vehicle’s raw point cloud with null vectors representing features of *MoDAR* points, which are boxes’ size, heading, score, and class
- *MoDAR* points with null vectors representing features of points in the ego vehicle’s raw point cloud which are points’ intensity and time-lag.

Once exchanged *MoDAR* points and the point cloud of the ego vehicle are merged, the result can be processed by the single-vehicle model developed in the Sec.III-A2 without changing its architecture.

IV. EXPERIMENTS AND RESULTS

A. Single-Vehicle Perception

1) *Datasets and Metrics*: As point clouds’ resolution exerts a large impact on the performance of LiDAR-based models, we test our model on three resolutions: 16, 32, and 64. While 32-channel and 64-channel point clouds are readily available in *NuScenes* dataset [2] and *KITTI* dataset [17] respectively, to the best of our knowledge, there are no publicly available datasets containing 16-channel point clouds. As a result, we synthesize a 16-channel dataset from the *NuScenes* dataset using the downsampling approach of [30].

a) *The NuScenes dataset*: is made of 850 20-second scenes split into 700 scenes for training and 150 scenes for validation. Each scene comprises data samples collected by a multimodal sensor suite including a 32-beam LiDAR operating at 20 Hz. In *NuScenes*’ convention, a keyframe is established once all sensors are in sync which happens every half a second. For each keyframe, objects are annotated as 3D bounding boxes. In addition, each object is assigned a unique ID that is kept consistent throughout a scene which enables us to generate the ground truth for the *rectification transformation* and scene flow. The downsampling of each point cloud in the *NuScenes* dataset to synthesize a 16-channel one is done by first identifying its points’ beam index via K-mean (K is 32 in the case of *NuScenes*) clustering on their azimuth coordinate, then assigning an equivalent beam index with respect to 16-channel LiDAR. More details can be found in [30]. Hereon, we refer to this synthesized dataset as *NuScenes-16*.

b) *The KITTI dataset*: ’s 3D Object Detection partition contains 7481 and 7581 samples for training and testing. Each sample comprises sensory measurements collected by a 64-beam LiDAR operating at 10Hz and several cameras. A common practice when working with *KITTI* is to split the original training data into 3712 training samples and 3769 validation samples for experimental studies. A challenge we encounter when using *KITTI* is that its 3D Object Detection partition contains temporally disjointed samples, thus being not straightforward to obtain input (point cloud sequences) and ground truth (scene flow) for our model. We resolve this challenge by matching samples in the 3D Object Detection partition with *KITTI*’s raw sequences. Since there are a few raw sequences that do not have *tracklet* annotation, meaning objects are not tracked, we only retain data samples whose associated raw sequences have *tracklets* (i.e., trajectories of objects) in the training set and validation set.

c) *Metrics*: We use mean Average Precision (mAP) to measure the performance of our model on the 3D object detection task. A prediction is matched with the ground truth that is closest, measured by an affinity, to it. A match is considered valid if the affinity is below a predefined threshold. For each threshold, the average precision is obtained by integrating the recall-precision curve for recall and precision above 0.1. The mAP is the mean of the average precision of the threshold set. For *NuScenes*, the affinity is the Euclidean distance on the ground plane between centers of predictions and ground truth. This distance has four thresholds: 0.5, 1.0, 2.0, and 4.0. For *KITTI*, the affinity is the Intersection-over-Union (IoU) in the BEV plane. Unlike *NuScenes*, *KITTI* uses only one affinity threshold for each class which is 0.7 for cars and 0.5 for pedestrians.

The evaluation of scene flow prediction is based on the set of standard metrics proposed by [31] which includes End-Point Error (EPE), strict/ relaxed accuracy (AccS/ AccR), and outlier (ROutliers). The EPE is the Euclidean distance between the predicted scene flow and their ground truth average over the total number of points. The AccS/ AccR is the percentage of points having either $EPE < 0.05/ 0.10$ meters or relative error $< 0.05/ 0.10$. The ROutliers is the percentage of points whose $EPE > 0.30$ meters and relative error > 0.30 .

2) *Experiments and Results*: The implementation of the single-vehicle perception model here follows the implementation made in our previous work [1] which uses the concatenation of 0.5-second point cloud sequences by EMC as the input. Since *NuScenes* and *KITTI* respectively obtain point clouds at 20 and 10 Hz, a 0.5-second sequence contains 10 and 5 point clouds. We use the same architecture, which uses PointPillar [22] as its backbone and CenterHead [4] as its RPN, for every experiment. In experiments on *NuScenes*, the detection range is limited to $[-51.2, 51.2]$ on the XY plane and $[-5.0, 3.0]$ along the Z axis. For experiments in *KITTI*, point clouds are first cropped using the left-color camera’s field of view as the annotations are only provided for objects that lie within the left-color camera’s image. The detection range on *KITTI* dataset is $[0, 69.12] \times [-39.68, 39.68] \times [-3, 1]$ along X, Y, and Z axis. Our implementation is based on the OpenPCDet [32]. The details on the model’s hyperparameters can be found in our code release.

The evaluation of the *Aligner++* on scene flow estimation task is done using the *NuScenes* dataset. The result shown in Tab.I indicates a significant improvement compared to our previous work [1] that reaches a state-of-art on accuracy-related metrics namely AccS, AccR, and ROutliers while maintaining low inference time. However, we have relatively high EPE this is because the evaluation is done for every point in the point cloud. This means the evaluation is carried out for both ground truth foreground points which have associated ground truth scene flow (can be nonzero or zero depending on dynamic) and ground truth background points which we assign the null vector as ground truth scene flow. Since the classification module of the Object Head inevitably makes false positive/ false negative foreground predictions, a number of background/ foreground points are predicted to have nonzero/ zero scene flow. Even though the portion of false

predictions is small, as indicated by accuracy (AccS, AccR) and outlier metrics, the magnitude of their error is sufficiently large, due to the fact either the prediction or ground truth is zero, thus resulting in a large EPE.

TABLE I
PERFORMANCE OF OUR MODEL ON SCENE FLOW METRICS

Method	EPE \downarrow	AccS \uparrow	AccR \uparrow	ROutliers \downarrow	Runtime \downarrow
FLOT [33]	1.216	3.0	10.3	63.9	2.01
NSFPrior [34]	0.707	19.3	37.8	32.0	63.46
PPWC-Net [35]	0.661	7.6	24.2	31.9	0.99
WsRSF [36]	0.539	17.9	37.4	22.9	1.46
PCAccumulation [37]	0.301	<u>26.6</u>	<u>53.4</u>	<u>12.1</u>	0.25
Aligner [1]	<u>0.506</u>	16.8	30.2	33.8	0.09
Aligner++	0.616	46.4	66.6	6.8	<u>0.10</u>

The better scene flow estimation made by the results in a higher detection accuracy on the *NuScenes* dataset which can be seen in Tab.II. The integration of *Aligner++*, made of HD Map and distillation using the teacher-student framework, improves the mAP average over 10 classes of objects of a plain PointPillar by 6 points which is almost double the gain brought by *Aligner* (3.4 points). Interestingly, the distillation is responsible for most (5.6 out of 6 points) of the success of the *Aligner++*.

TABLE II
DETECTION IMPROVEMENT DUE TO OUR EXTENSION

PointPillar	Aligner [1]	HD Map	Distilling Oracle	mAP (avg 10 classes)
✓				39.0
✓	✓			42.4
✓		✓		39.4
✓		✓	✓	45.0

The robustness of our *Aligner++* is demonstrated by experiments on the *KITTI* and the synthetic *NuScenes-16* dataset. As can be seen Tab.III and Tab.IV, the integration of *Aligner++* consistently improves the accuracy of detecting objects in point cloud sequences. A common point between these two tables is that performance gain amounts to the *Aligner++* is larger for vehicle-like classes (e.g., car, truck, or trailer). This is because the scene flow ground truth is generated using the *rectification transformation* (2) which is established based on the rigid motion assumption. This assumption holds for vehicle-like classes while being an oversimplification for pedestrians. As a result, the estimation of scene flow for vehicle-like classes is more accurate, thus higher detection accuracy. Another important result can be drawn from Tab.III and Tab.IV is that the effectiveness, in terms of detection accuracy, of using point cloud sequences over single point clouds persists on various LiDAR resolutions.

B. V2X Collaborative Perception - Experiments

1) *Dataset and Metric*: To evaluate our collaboration framework, we use the V2X-Sim 2.0 [18] which is made using CARLA and the traffic simulator SUMO. This dataset is made of 100 100-frame sequences of traffic taking place

TABLE III
DETECTION PERFORMANCE ON KITTI DATASET

Class	Model	Sequence Length			
		1	2	3	4
Car	PointPillar	66.54	70.44	69.66	69.88
	+ Aligner++	/	+3.91	+7.45	+6.3
Pedestrian	PointPillar	5.32	6.16	16.71	20.77
	+ Aligner++	/	+4.82	+4.07	+3.6

TABLE IV
DETECTION PERFORMANCE ON NUSCENES-16

Model	PointPillar		PointPillar + Aligner++
	Seq Length	1	10
Car	56.14	79.84	80.81
Truck	26.99	48.64	49.39
Const. Vehicle	0.61	8.21	9.45
Bus	38.06	59.91	59.99
Trailer	11.05	26.15	29.03
Barrier	38.02	59.07	59.26
Motorcycle	12.70	41.14	41.72
Bicycle	0.11	15.22	18.40
Pedestrian	45.57	76.13	76.64
Traffic Cone	33.04	54.66	54.51
mAP (avg. 10 classes)	26.23	46.90	47.92

at intersections of three towns of CARLA which are Town 3, Town 4, and Town 5. Each sequence contains data samples recorded at 5 Hz. Each data sample comprises raw sensory measurements made by the ego vehicle, one to four CAVs, and an IRSU, which is placed at an elevated position that has a large minimally occluded field of view of the intersection. Every vehicle and the IRSU are equipped with a 32-channel LiDAR. All agents are in sync which results in the same timestamp of data that they collect.

The V2X-Sim 2.0 dataset provides object annotations for each data sample. The official training, validation, and testing split are made of temporally disjoint data samples from three towns chosen such that there is no overlap in terms of intersections. Since we need point cloud sequences as input to our models, we can't use the official splits. Instead, we use sequences in Town 4 and Town 5 as the training set, and those in Town 3 as the validation set, thus ensuring there is no intersection overlap. This choice results in an 8900-data-sample training set and an 1100-data-sample validation set. Since this dataset follows the format of the NuScenes, we use NuScenes' implementation of mean Average Precision (mAP) (details in Sec.IV-A1c) to measure the performance of our framework and baselines.

2) *Implementation, Experiments and Results*: In the convention of the V2X-Sim dataset, the IRSU and the ego vehicle are respectively assigned the id of 0 and 1 while other CAVs get id ranging from 2 to 5. To test our collaboration method's ability to handle asynchronous exchanged information, we set the time lag between the timestamp t of the ego vehicle's query and the timestamp t_i of the detection $\mathcal{B}_i = \{\mathbf{b}_{i,j}\}$ made by agent $\mathcal{A}_i (i \in \{0, 2, 3, 4, 5\})$ to the time gap between two

consecutive data sample of V2X-Sim which is 0.2 seconds.

We benchmark our approach to collaborative perception against two extremes of the performance-bandwidth spectrum which are Late and Early collaboration. **Late Collaboration** achieves the minimal bandwidth usage by fusing the detection $\mathcal{B}_1 = \{\mathbf{b}_{1,j}\}_{j=1}^{|\mathcal{B}_1|}$ made by the ego vehicle with the detection made by other agents $\{\mathcal{B}_i | i \in \{0, 2, 3, 4, 5\}\}$ using Non-Max Suppression. We evaluate this baseline under three settings including

- *asynchronous* exchange where the gap between t_i and t is 0.2 seconds as described above
- *asynchronous* exchange with \mathcal{B}_i propagated from t_i to t using scene flow by the procedure described in section III-B2
- *synchronous* exchange where there is no gap between t and t_i

On the other hand, **Early Collaboration** reaches high performance by exchanging the entire raw point cloud sequences $\mathcal{S}_i = \{\mathcal{P}_i^{t_i-K+1}, \dots, \mathcal{P}_i^{t_i}\}$ collected by each agent \mathcal{A}_i is the second baseline. To explore the upper bound of V2X collaborative perception, we only apply the *synchronous* exchange to this baseline.

In the implementation of our V2X collaboration framework, every agent uses the single-vehicle detection model that is developed in Sec.III-A2 with the absence of the teacher module. The architecture and hyper-parameters are kept unchanged as the experiments of the single-vehicle model in Sec.IV-A2. While previous works using the V2X-Sim dataset [14], [18] set the detection range to $[-32, 32]$ meters along the X and Y axis, centered on the ego vehicle, we extend this range to $[-51.2, 51.2]$ to better demonstrate the performance gain thanks to collaborative perception via V2X.

To verify the ability of enhancing single-vehicle perception of V2X collaboration, we evaluate our approach and baselines in the setting where ground truths are made of objects visible to the ego vehicle meaning their bounding boxes contain at least one point of the point cloud \mathcal{P}_e^t , which the ego vehicle obtained at the time step of query t . The result of this evaluation is summarized in Tab.V which shows that late collaboration in all three settings is not beneficial, as the best late collaboration is 4.42 mAP behind the single-agent perception. This is because True Positive (TP) detections made by other agents are counted as false positives if they are not visible to the ego vehicle. In addition, ill-localized but overly confident detections made by other agents can suppress good detections made by the ego vehicle, thus further reducing the overall performance. Remarkably, our collaboration approach using *MoDAR* points outperforms the early collaboration by 3.35 mAP while consuming the same amount of bandwidth as late collaboration. This reaffirms our design philosophy that *a good multi-agent collaborative perception framework can be made on the foundation of a good single-agent perception model and a simple collaboration method*.

Beside enabling the ego vehicle more accurately detecting objects that are visible to itself, another great benefit of collaborative perception is to help the ego vehicle see the invisible objects - those do not contain any points of its

TABLE V
PERFORMANCE OF COLLABORATION METHODS ON GROUND TRUTH THAT ARE VISIBLE TO THE EGO VEHICLE

Collaboration Method	mAP	Exchanged Info Size (MByte)
None	65.71	0
Late - <i>async</i>	54.77	0.01
Late - <i>async prop.</i>	59.34	0.01
Late - <i>sync</i>	61.29	0.01
Mid - DiscoNet	69.98	-
Early	71.84	33.95
Ours - <i>MoDAR</i>	75.19	0.01

point cloud \mathcal{P}_e^t , thus overcoming the challenge of occlusion and sparsity. To demonstrate this, we perform the relax the criterion of eligibility of ground truth such that they only need to contain at least one point emitted by any agents in the V2X network. The performance shown in Tab.VI indicates that on a larger set of ground truths, Late Collaboration does improve performance, compared to single-vehicle (no collaboration). The improvement is significant (at least 8.35 mAP) even in the poorest setting where the set of exchanged detection $\{\mathcal{B}_i | i \in \{0, 2, 3, 4, 5\}\}$ is 0.2 seconds behind the time of query, thus resulting a spatial misalignment between detected objects that are exchanged and their associated ground truths if the underlying objects are dynamic. This can be explained by a significant number of static and slow-moving objects present in an intersection whose past detections remain true positive at the present. When detections of dynamic objects are better accounted for as in the *sync* setting where agents exchange their detections at the same timestamp as the query, the performance is largely improved by 9.29 mAP, compared to the *async* setting. However, this *sync* setting is unrealistic because different agents have different detection rates. Interestingly, propagating detections using scene flow as in the *async prop.* setting can reach 96.20% the performance of the *sync* setting (2.68 mAP behind). This implies the effectiveness of scene flow estimated by our *Aligner++*. In this setting, our collaboration method using *MoDAR* no longer outperforms the early collaboration baseline as some distant objects (with respect to the ego vehicle) are inevitably missed by connected agents, thus remaining invisible to the ego vehicles and being unable to be detected. However, our method still maintain favorable performance of 98.2% of the early collaboration's while attaining as low bandwidth usage as late collaboration.

REFERENCES

- [1] M.-Q. Dao, V. Frémont, and E. Héry, “Aligning bird-eye view representation of point cloud sequences using scene flow,” *arXiv preprint arXiv:2305.02909*, 2023.
- [2] H. Caesar, V. Bankiti, A. H. Lang, S. Vora, V. E. Liou, Q. Xu, A. Krishnan, Y. Pan, G. Baldan, and O. Beijbom, “nuscenes: A multimodal dataset for autonomous driving,” in *Proceedings of the IEEE/CVF conference on computer vision and pattern recognition*, 2020, pp. 11 621–11 631.
- [3] Y. Hu, Z. Ding, R. Ge, W. Shao, L. Huang, K. Li, and Q. Liu, “Afdetv2: Rethinking the necessity of the second stage for object detection from point clouds,” in *Proceedings of the AAAI Conference on Artificial Intelligence*, vol. 36, no. 1, 2022, pp. 969–979.

TABLE VI

PERFORMANCE OF COLLABORATION METHODS ON GROUND TRUTH THAT ARE VISIBLE TO AT LEAST ONE AGENTS

Collaboration Method	mAP
None	52.84
Late - <i>async</i>	61.19
Late - <i>async</i> prop.	67.80
Late - <i>sync</i>	70.48
Early	78.10
Ours - MoDAR	76.72
Ours - MoDAR and Foreground	75.41

[4] T. Yin, X. Zhou, and P. Krahenbuhl, “Center-based 3d object detection and tracking,” in *Proceedings of the IEEE/CVF conference on computer vision and pattern recognition*, 2021, pp. 11 784–11 793.

[5] N. Djuric, H. Cui, Z. Su, S. Wu, H. Wang, F.-C. Chou, L. San Martin, S. Feng, R. Hu, Y. Xu *et al.*, “Multixnet: Multiclass multistage multimodal motion prediction,” in *2021 IEEE Intelligent Vehicles Symposium (IV)*. IEEE, 2021, pp. 435–442.

[6] A. Laddha, S. Gautam, S. Palombo, S. Pandey, and C. Vallespi-Gonzalez, “Mvfusenet: Improving end-to-end object detection and motion forecasting through multi-view fusion of lidar data,” in *Proceedings of the IEEE/CVF Conference on Computer Vision and Pattern Recognition*, 2021, pp. 2865–2874.

[7] D. Tsai, J. S. Berrio, M. Shan, E. Nebot, and S. Worrall, “Ms3d: Leveraging multiple detectors for unsupervised domain adaptation in 3d object detection,” *arXiv preprint arXiv:2304.02431*, 2023.

[8] Z. Yang, Y. Zhou, Z. Chen, and J. Ngiam, “3d-man: 3d multi-frame attention network for object detection,” in *Proceedings of the IEEE/CVF conference on computer vision and pattern recognition*, 2021, pp. 1863–1872.

[9] Y. Li, C. R. Qi, Y. Zhou, C. Liu, and D. Anguelov, “Modar: Using motion forecasting for 3d object detection in point cloud sequences,” in *Proceedings of the IEEE/CVF Conference on Computer Vision and Pattern Recognition*, 2023, pp. 9329–9339.

[10] X. Chen, S. Shi, B. Zhu, K. C. Cheung, H. Xu, and H. Li, “Mppnet: Multi-frame feature intertwining with proxy points for 3d temporal object detection,” in *European Conference on Computer Vision*. Springer, 2022, pp. 680–697.

[11] W. Luo, B. Yang, and R. Urtasun, “Fast and furious: Real time end-to-end 3d detection, tracking and motion forecasting with a single convolutional net,” in *Proceedings of the IEEE conference on Computer Vision and Pattern Recognition*, 2018, pp. 3569–3577.

[12] M. Schwall, T. Daniel, T. Victor, F. Favaro, and H. Hohnhold, “Waymo public road safety performance data,” *arXiv preprint arXiv:2011.00038*, 2020.

[13] T.-H. Wang, S. Manivasagam, M. Liang, B. Yang, W. Zeng, and R. Urtasun, “V2vnet: Vehicle-to-vehicle communication for joint perception and prediction,” in *Computer Vision–ECCV 2020: 16th European Conference, Glasgow, UK, August 23–28, 2020, Proceedings, Part II 16*. Springer, 2020, pp. 605–621.

[14] Y. Li, S. Ren, P. Wu, S. Chen, C. Feng, and W. Zhang, “Learning distilled collaboration graph for multi-agent perception,” *Advances in Neural Information Processing Systems*, vol. 34, pp. 29 541–29 552, 2021.

[15] R. Xu, H. Xiang, Z. Tu, X. Xia, M.-H. Yang, and J. Ma, “V2x-vit: Vehicle-to-everything cooperative perception with vision transformer,” in *Computer Vision–ECCV 2022: 17th European Conference, Tel Aviv, Israel, October 23–27, 2022, Proceedings, Part XXXIX*. Springer, 2022, pp. 107–124.

[16] R. Xu, J. Li, X. Dong, H. Yu, and J. Ma, “Bridging the domain gap for multi-agent perception,” *arXiv preprint arXiv:2210.08451*, 2022.

[17] A. Geiger, P. Lenz, and R. Urtasun, “Are we ready for autonomous driving? the kitti vision benchmark suite,” in *2012 IEEE conference on computer vision and pattern recognition*. IEEE, 2012, pp. 3354–3361.

[18] Y. Li, D. Ma, Z. An, Z. Wang, Y. Zhong, S. Chen, and C. Feng, “V2x-sim: Multi-agent collaborative perception dataset and benchmark for autonomous driving,” *IEEE Robotics and Automation Letters*, vol. 7, no. 4, pp. 10 914–10 921, 2022.

[19] H. Yu, Y. Luo, M. Shu, Y. Huo, Z. Yang, Y. Shi, Z. Guo, H. Li, X. Hu, J. Yuan *et al.*, “Dair-v2x: A large-scale dataset for vehicle-infrastructure cooperative 3d object detection,” in *Proceedings of the IEEE/CVF Conference on Computer Vision and Pattern Recognition*, 2022, pp. 21 361–21 370.

[20] M. Jaderberg, K. Simonyan, A. Zisserman *et al.*, “Spatial transformer networks,” *Advances in neural information processing systems*, vol. 28, 2015.

[21] R. Xu, Z. Tu, H. Xiang, W. Shao, B. Zhou, and J. Ma, “Cobevt: Cooperative bird’s eye view semantic segmentation with sparse transformers,” *arXiv preprint arXiv:2207.02202*, 2022.

[22] A. H. Lang, S. Vora, H. Caesar, L. Zhou, J. Yang, and O. Beijbom, “Pointpillars: Fast encoders for object detection from point clouds,” in *Proceedings of the IEEE/CVF conference on computer vision and pattern recognition*, 2019, pp. 12 697–12 705.

[23] Y. Zhou and O. Tuzel, “Voxelnet: End-to-end learning for point cloud based 3d object detection,” in *Proceedings of the IEEE conference on computer vision and pattern recognition*, 2018, pp. 4490–4499.

[24] K. Vedder and E. Eaton, “Sparse pointpillars: Maintaining and exploiting input sparsity to improve runtime on embedded systems,” in *2022 IEEE/RSJ International Conference on Intelligent Robots and Systems (IROS)*. IEEE, 2022, pp. 2025–2031.

[25] Y. Yan, Y. Mao, and B. Li, “Second: Sparsely embedded convolutional detection,” *Sensors*, vol. 18, no. 10, p. 3337, 2018.

[26] B. Yang, M. Liang, and R. Urtasun, “Hdnet: Exploiting hd maps for 3d object detection,” in *Conference on Robot Learning*. PMLR, 2018, pp. 146–155.

[27] J. Fang, D. Zhou, X. Song, and L. Zhang, “Mapfusion: A general framework for 3d object detection with hdmaps,” in *2021 IEEE/RSJ International Conference on Intelligent Robots and Systems (IROS)*. IEEE, 2021, pp. 3406–3413.

[28] X. Weng, J. Wang, D. Held, and K. Kitani, “Ab3dmot: A baseline for 3d multi-object tracking and new evaluation metrics,” *arXiv preprint arXiv:2008.08063*, 2020.

[29] B. Varadarajan, A. Hefny, A. Srivastava, K. S. Refaat, N. Nayakanti, A. Cornman, K. Chen, B. Douillard, C. P. Lam, D. Anguelov *et al.*, “Multipath++: Efficient information fusion and trajectory aggregation for behavior prediction,” in *2022 International Conference on Robotics and Automation (ICRA)*. IEEE, 2022, pp. 7814–7821.

[30] Y. Wei, Z. Wei, Y. Rao, J. Li, J. Zhou, and J. Lu, “Lidar distillation: bridging the beam-induced domain gap for 3d object detection,” in *Computer Vision–ECCV 2022: 17th European Conference, Tel Aviv, Israel, October 23–27, 2022, Proceedings, Part XXXIX*. Springer, 2022, pp. 179–195.

[31] X. Liu, C. R. Qi, and L. J. Guibas, “Flownet3d: Learning scene flow in 3d point clouds,” in *Proceedings of the IEEE/CVF Conference on Computer Vision and Pattern Recognition*, 2019, pp. 529–537.

[32] O. D. Team, “Openpcdet: An open-source toolbox for 3d object detection from point clouds,” <https://github.com/open-mmlab/OpenPCDet>, 2020.

[33] G. Puy, A. Boulch, and R. Marlet, “Flot: Scene flow on point clouds guided by optimal transport,” in *European conference on computer vision*. Springer, 2020, pp. 527–544.

[34] X. Li, J. Kaesemodel Pontes, and S. Lucey, “Neural scene flow prior,” *Advances in Neural Information Processing Systems*, vol. 34, pp. 7838–7851, 2021.

[35] W. Wu, Z. Y. Wang, Z. Li, W. Liu, and L. Fuxin, “Pointpwc-net: Cost volume on point clouds for (self-) supervised scene flow estimation,” in *European conference on computer vision*. Springer, 2020, pp. 88–107.

[36] Z. Gojcic, O. Litany, A. Wieser, L. J. Guibas, and T. Birdal, “Weakly supervised learning of rigid 3d scene flow,” in *Proceedings of the IEEE/CVF conference on computer vision and pattern recognition*, 2021, pp. 5692–5703.

[37] S. Huang, Z. Gojcic, J. Huang, A. Wieser, and K. Schindler, “Dynamic 3d scene analysis by point cloud accumulation,” in *European Conference on Computer Vision*. Springer, 2022, pp. 674–690.